

**Aerodynamics E3 Coursework: A Report on the Supersonic Flow and Propulsion
Laboratories**

Philip Beswick @00662943

The University of Salford

Aerodynamics E3

Dr Andreea Koreanschi, Dr Ali Bahr Ennil

25/03/25

Abstract

This report consists of two distinct elements. Part 1 discusses the Supersonic Wind Tunnel laboratory, which aims to investigate how shockwaves form on a diamond shaped airfoil at various angles of attacks, which then compares with the known Supersonic wave theory. Part 2 discusses tests completed on the SR-30 turbojet engine located in the Aero/Mechanical Laboratory at the University of Salford. Both parts proved to be successful as each provided results that could be disucssed. Although not all results were valid, they were easily to explain and identify, using the known theory of supersonic shocks and the Brayton Cycle respectively. Ultimately, in part 1, shock waves were observed over the airfoil, which were then compared with calcualted shock angles and in part 2 the equipment was able to measure the thrust output of the SR-30, which was then comapred with a calcualted value. If further study were to be compelted, a more indepth analysis of the SR-30 would be useful in order to understand why the measured values of thrust were not as expected.

**Aerodynamics E3 Coursework: A Report on the Supersonic Flow and Propulsion
Laboratories**

Contents

List of Figures	4
List of Tables	4
List of Equations	4
1 Supersonic Flow Laboratory	6
1.1 Aims and Objectives	6
1.2 Description of Theoretical Expectations	6
1.3 Description of Experimental Procedure	6
1.4 Description of Experimental Outcomes	7
1.5 Discussion	14
2 Propulsion Laboratory	16
2.1 Aims and Objectives	16
2.2 Equipment Description	16
2.3 Experimental Methodology	16
2.4 Experimental Observations	17
2.5 Experimental Data	18
2.6 Post-Processing Methodology	26
2.7 Discussion	26
2.8 Conclusions	28
3 Appendix	29
References	30

List of Figures

1.1	The Schlieren Image Produced at an Angle of Attack of 0°	8
1.2	The Schlieren Image Produced at an Angle of Attack of 2°	9
1.3	The Schlieren Image Produced at an Angle of Attack of 4°	10
1.4	The Schlieren Image Produced at an Angle of Attack of 6°	11
1.5	The Schlieren Image Produced at an Angle of Attack of 8°	12
1.6	Pressure Distribution for various Angles of Attack	14
2.1	This graph shows the relationship between the RPM of the SR-30 and it's Isentropic Efficiency	18
2.2	This graph shows the relationship between the Pressure Ratio of the SR-30 and it's Isentropic Efficiency	19
2.3	This graph shows the relationship between the entropy drop in the compressor and the exit temperature of the compressor.	20
2.4	This graph shows the relationship between the RPM of the SR-30 and it's Brayton Cycle Efficiency	21
2.5	This graph shows the relationship between the RPM of the SR-30 and it's Measured Thrust	22
2.6	This graph shows the relationship between the RPM of the SR-30 and it's TSFC	23
2.7	This graph shows the relationship between the RPM of the SR-30 and it's Nozzel Exit Mach Number.	24
2.8	This graph shows the relationship between the RPM of the SR-30 and it's Inlet Mass Flow Rate	25

List of Tables

1.1	Values of pressure with varying angle of attack at each pressure tapping point.	13
1.2	Calculated values of shock angles	15
2.1	This table shows the values of thrust for the SR-30, both measured and calculated with increasing RPM.	25

List of Equations

1.1	Equation to find shock angles.	15
2.1	Equation to find Isentropic Efficiency	26
2.2	Equation to find Thrust	26
2.3	Equation to find Mass Flow Rate.	26
2.4	Equation to find airspeed.	26

1 Supersonic Flow Laboratory

1.1 Aims and Objectives

The procedure aims to use a Schlieren system to observe the shockwave structures on a diamond aerofoil when orientated at different angles of attack but in a constant air flow of Mach 1.8. Objectives of this procedure include obtaining numerical and physical results that can be compared with theory and gaining technical skills, such as familiarity with the equipment used.

1.2 Description of Theoretical Expectations

As the diamond airfoil has been placed in a flow regime where the freestream Mach number is 1.8, shock waves will be expected to form. These shocks will form about the leading edge point, trailing edge point and expansion fans at the shoulders of the diamond airfoil. Furthermore, in *Aerodynamics*, Clancy suggests that with an increasing angle of attack, the shocks may become detached from the leading edge(Clancy, 1986). To keep the shocks attached to the leading edge, the free stream Mach number would have to increase; in this procedure, this remains constant. When the angle of attack further increases, a bow, detached shock is expected to occur ahead of the leading edge(Clancy, 1986).

1.3 Description of Experimental Procedure

Before the testing of the diamond airfoil at different angles of attacks can take place, the supersonic wind tunnel must be prepared. Preparation involves:

- Fitting the appropriate liner to the tunnel to achieve the desired free stream Mach number (in this case, a liner to achieve Mach 1.8 was attached).
- The model must be secured in the tunnel's testing section.
- The Schlieren apparatus must be set up.

Once this has been completed, the angle of attack of the model must be set by the tunnel operators, and then the tunnel bypass valve can be opened. Then, the tunnel vacuum pump can be started and once it reaches full speed, the bypass valve should again be shut. At this stage, pressure and Mach numbers were recorded for the tunnel at 25 different pressure tapping

points. This data is then saved to a spreadsheet for post-processing. Concurrently, the Schlieren apparatus will be displaying the model and (if present) any shocks that are occurring. Once all data has been collected, the bypass valve is opened, the tunnel is stopped and these steps previously outlined are repeated for the following angles of attacks: 0 degrees, 2 degrees, 4 degrees, 6 degrees and 8 degrees.

1.4 Description of Experimental Outcomes

Upon completion of the procedure, Schlieren images for each angle of attack were recorded. These can be found in Figures 1.1 to 1.5.

Figure 1.1

The Schlieren Image Produced at an Angle of Attack of 0° .

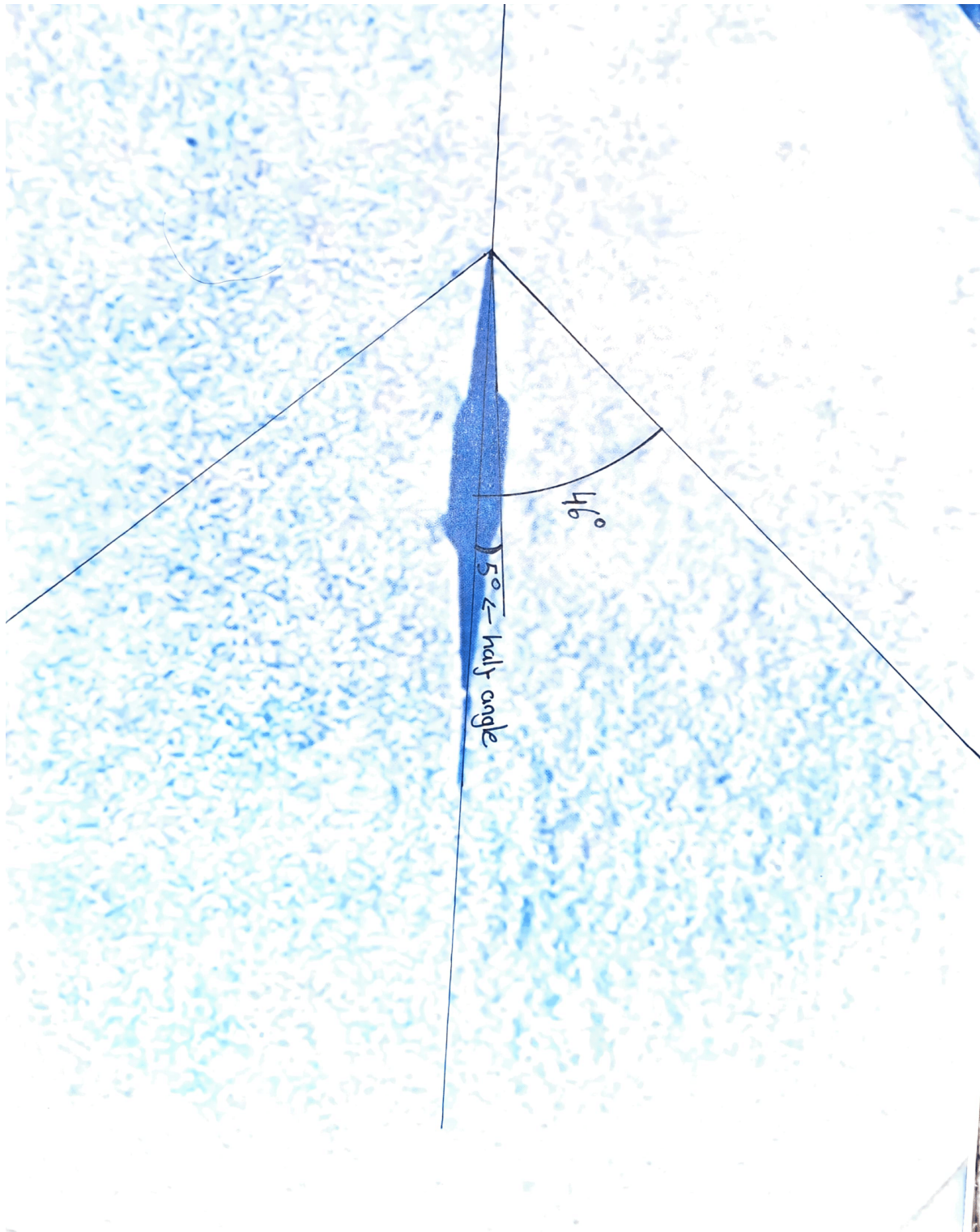


Figure 1.2

The Schlieren Image Produced at an Angle of Attack of 2° .

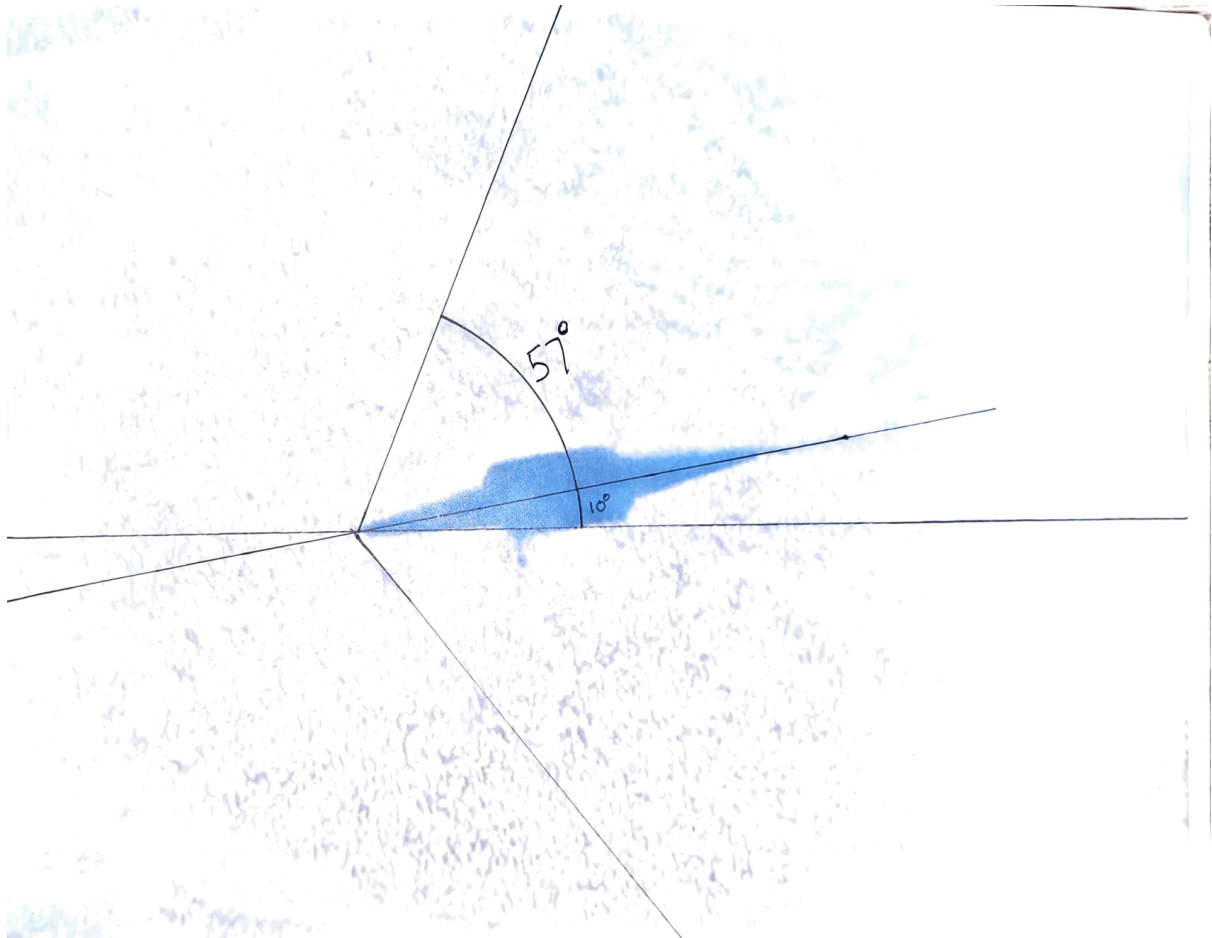


Figure 1.3

The Schlieren Image Produced at an Angle of Attack of 4° .

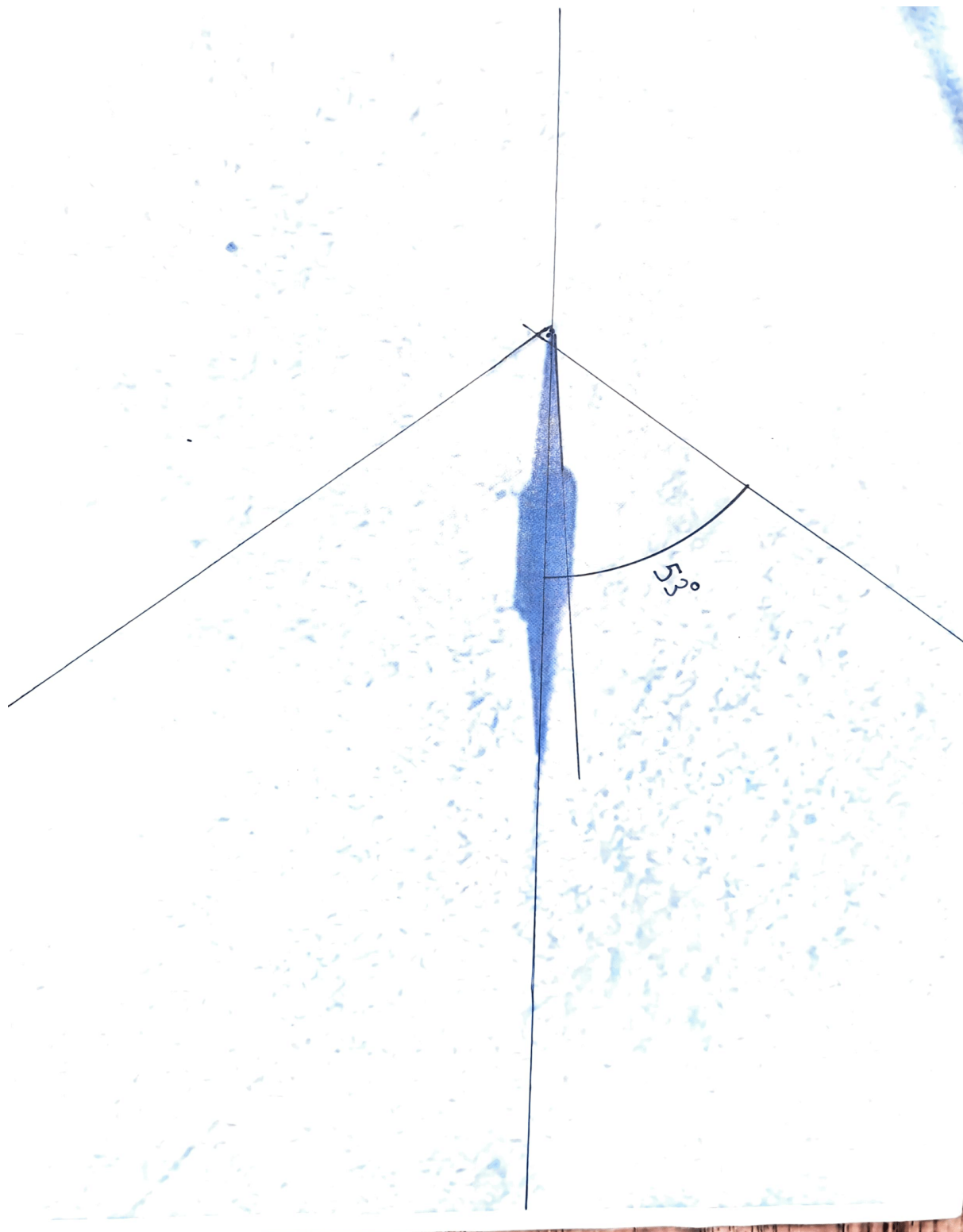


Figure 1.4

The Schlieren Image Produced at an Angle of Attack of 6° .

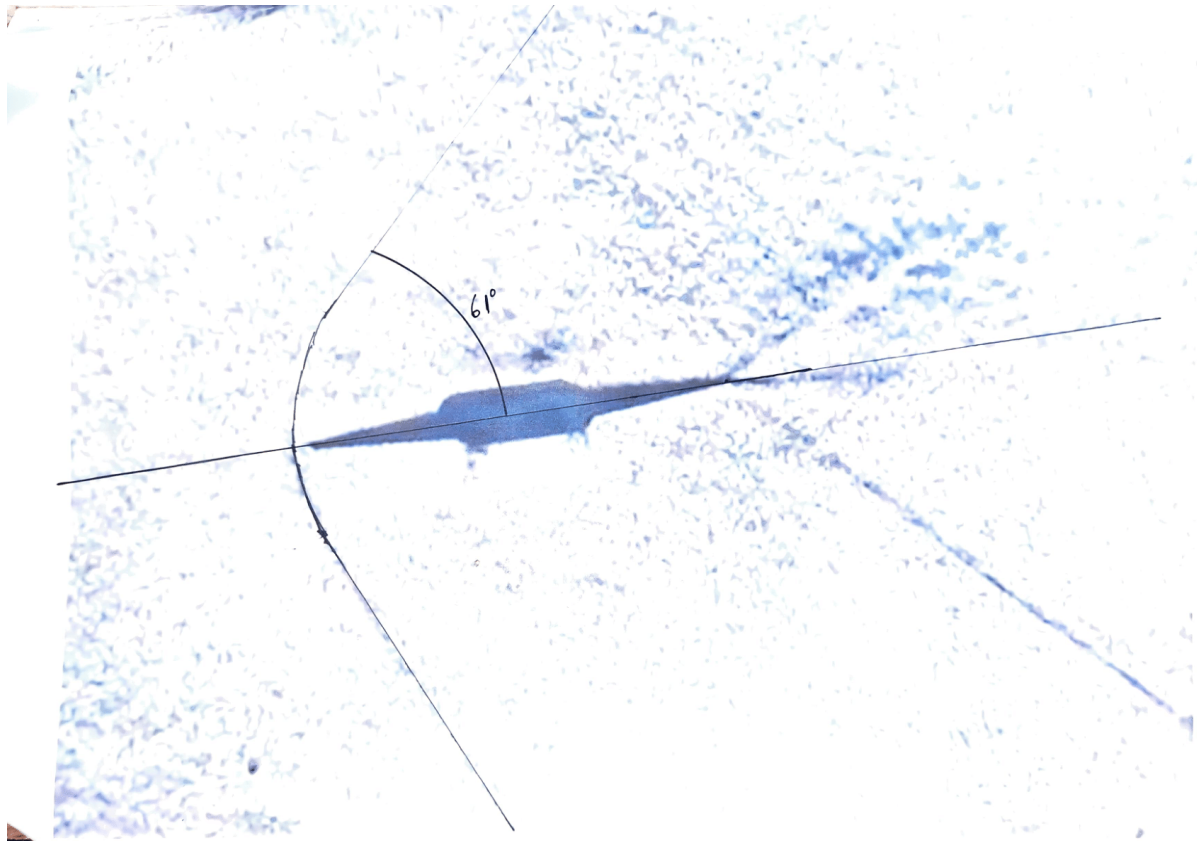
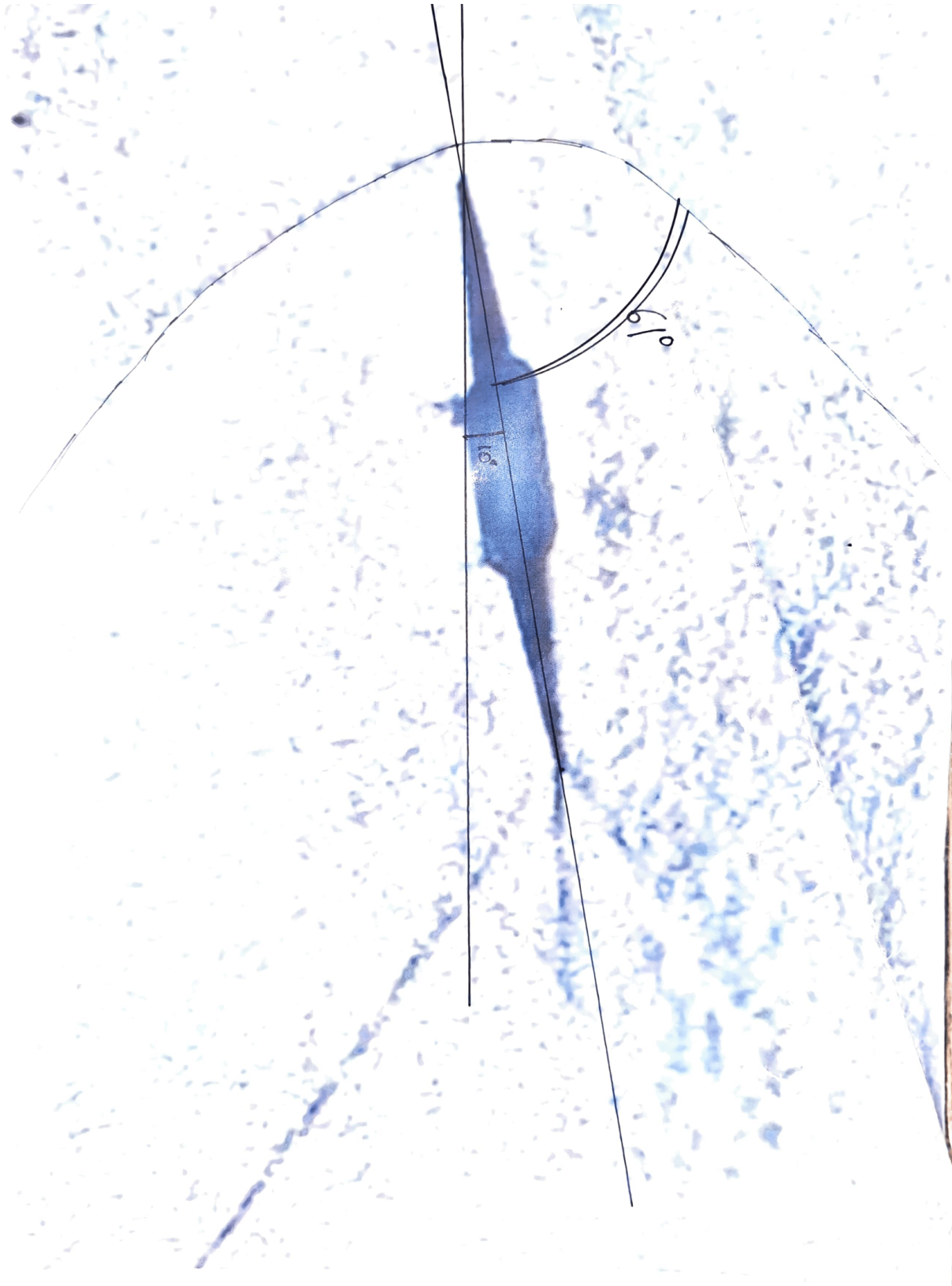


Figure 1.5

The Schlieren Image Produced at an Angle of Attack of 8° .



These figures show that as angle of attack increases, the shock angle also increases,

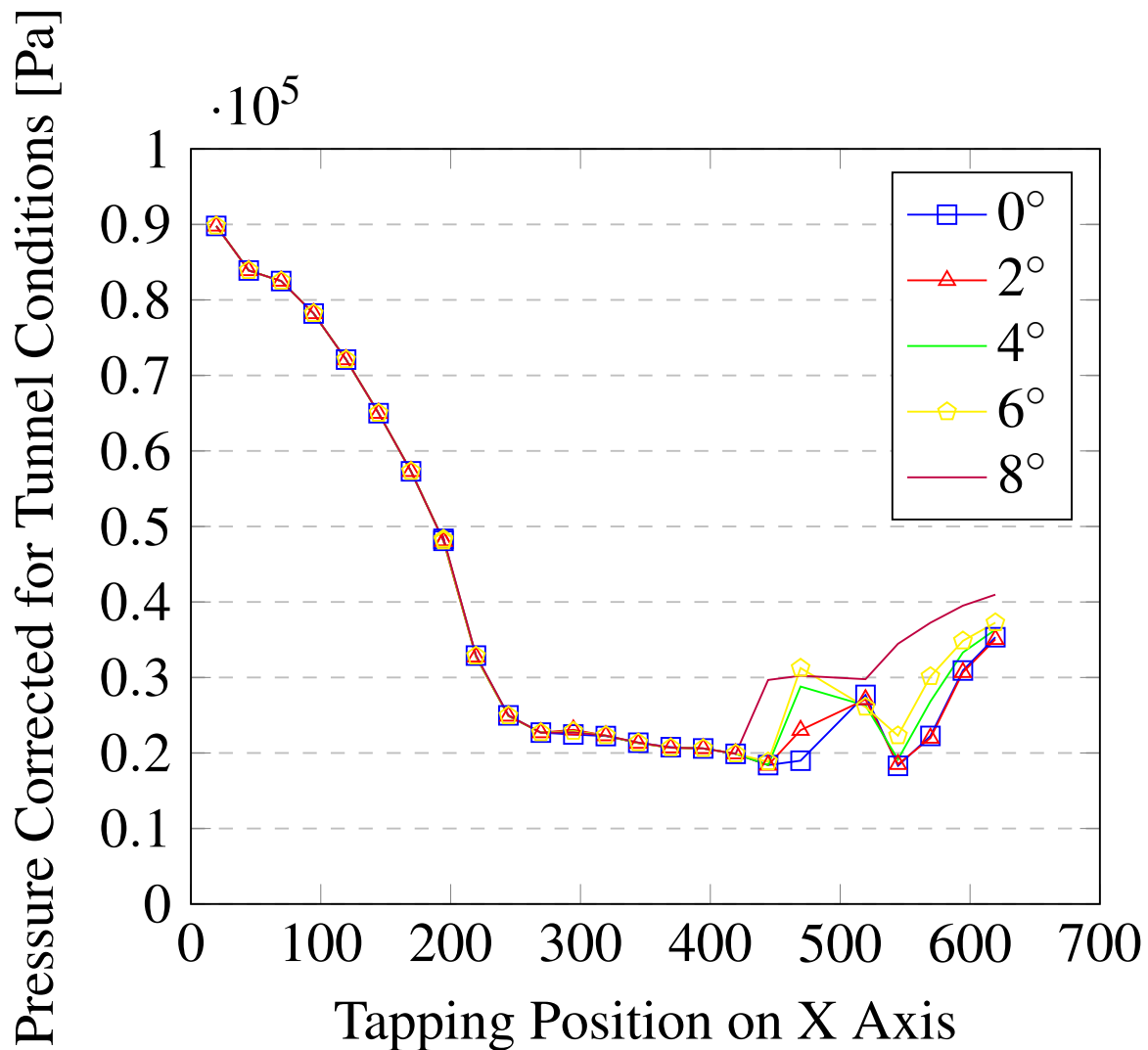
although there are anomalous results for angles of 2° and 4° . In addition to the Schlieren images produced, values of local pressure were taken at 25 unique points in the tunnel's testing section. These results can be found in Table 1.1.

Table 1.1

Values of pressure with varying angle of attack at each pressure tapping point.

Model Angle	Corrected Pressures (Pa)																								
(degrees)	1	2	3	4	5	6	7	8	9	10	11	12	13	14	15	16	17	18	19	20	21	22	23	24	25
0	89800	83900	82500	78200	72100	65000	57300	48100	48360	32900	24980	22700	22450	22240	21360	20770	20600	19890	18400	18980	27690	18300	22260	30920	35330
2	89800	83900	82500	78200	72100	65000	57300	48100	48060	32740	24900	22700	23070	22300	21300	20700	20600	19900	18400	23020	27090	18500	21980	30680	35050
4.1	89800	83900	82500	78200	72100	65000	57300	48100	48230	32790	24900	22700	22890	22280	21330	20700	20600	19900	18410	28800	26290	19150	26830	33310	36340
5.9	89800	83900	82500	78200	72100	65000	57300	48100	48330	32850	24930	22700	22880	22310	21360	20700	20600	19900	18840	31250	26080	22290	30130	34850	37260
7.9	89800	83900	82500	78200	72100	65000	57300	48100	48430	32930	24970	22690	22740	22300	21380	20710	20600	19900	29670	30230	29770	34460	37250	39510	40970

The pressure distribution for each of the angles of attack measured can be found below in Figure 1.6.

Figure 1.6*Pressure Distribution for various Angles of Attack*

It is important to note that Figure 1.6 has the values of pressure that have been corrected accounting for atmospheric pressure and are therefore true, values of pressure for each pressure tapping location. The model is also tested upside down in the tunnel, hence the shape of the graph roughly appearing to be the mirror image of what is expected.

1.5 Discussion

Overall, the Schlieren images seen in Figures 1.1 to 1.5 do tend to match the theory suggested by Clancy in *Aerodynamics* (Clancy, 1986). As the angle of attack increases, the shocks both detach from the leading edge and become more similar to a bow shock, rather than a normal one. The only difference is that expansion fans are not present in the Schlieren

images. This is likely due to the small area of the testing section, which will prevent their development due to boundary layer conditions interfering with the flow around the diamond airfoil.

Table 1.2

Calculated values of shock angles

Model Angle	Free Steam Mach Number	Shock Angle
(degrees)	(Mach)	(degrees)
0	1.8	38.44
2	1.8	40.56
4.1	1.8	42.96
5.9	1.8	45.2
7.9	1.8	47.97

Also, the values of the calculated shock angle, seen in Table 1.2 are very different from the values measured in Figures 1.1 to 1.5. Again, the impact of the wind tunnel walls may result in different shock angles when measuring and calculating. The calculated values assume absolutely ideal conditions (steady, inviscid and adiabatic flow with no body forces), ultimately these are not realistic conditions when operating in a wind tunnel. In addition, the angles on the Schlieren images were measured by first taking a picture of the image displayed on a monitor, and then physically measuring with a protractor. Here, a great deal of inaccuracy has occurred, which will result in shock angles that are not absolutely correct. Therefore, it is likely that both methods have inaccuracies (although different in nature) and is therefore unsurprising why they therefore give different results. The shock angles were calculated using the relation between the flow angle, θ , the shock angle β and the flow freestream velocity, M which takes the value of 1.8.

$$\tan(\theta) = 2 \cot(\beta) \frac{M^2 \sin^2(\beta) - 1}{M^2(\gamma + \cos(2\beta) + 2)}, \quad (1.1)$$

The methodology for how this equation was applied will be discussed in the Appendix.

2 Propulsion Laboratory

2.1 Aims and Objectives

The experimental procedure conducted aims to produce data which can be used to analyse the performance of a small turbojet engine, while this report will discuss said data and suggest how effective the procedure was as a whole. The objectives of this laboratory are twofold:

1. To examine the performance of a small-scale turbojet engine operating at speeds up to 70000 rpm.
2. To gain a good understanding of the thermodynamic performance of a gas turbine engine operating on the Brayton cycle.

2.2 Equipment Description

The turbojet engine used in this procedure was the SR-30, which was mounted to the TTL Mini-Lab test bench. This engine has a centrifugal flow compressor, a reverse flow annular combustor and an axial flow turbine. Furthermore, it's powered by kerosene fuel. In addition, the engine is equipped with four thermocouple temperature sensors and four pressure sensors, which makes the analysis of the engine's performance possible. All data is collected by a connected computer, which monitors all of the previously mentioned sensors as well as fuel flow, thrust and RPM. The TTL Mini-Lab test bench controls the starting procedure of the engine as well as a lever, which controls the power (changes RPM) of the engine.

2.3 Experimental Methodology

Due to the potentially hazardous nature of this procedure, several precautions were taken to ensure the lab operated safely. These were:

- Ear protection (to EN352-2 standards) was worn at all times (British Standards Institution, 2020).
- No naked flames were used due to the flammable nature of the kerosene fuel.
- Safety covers were in place due to the high running speeds of the engine.

- The exhaust system was not approached due to the high temperature the engine runs at.
- The room was well ventilated due to the high oxygen use of the engine. All exhaust gasses were dispersed outside of the building.

As all health and safety precautions were undertaken, the operation of the SR-30 could proceed. A laboratory technician started the engine to achieve a steady, idle RPM. Once this has been achieved, the power handle on the TTL Mini-Lab bench is set to give an engine RPM of 50000. Once the engine is performing steadily at this speed, the computer is set to record data for 1 minute, the computer takes several readings during this time. This is repeated for speeds of 60000 RPM and 70000 RPM until the engine is set back to idle and then shut down.

2.4 Experimental Observations

As the procedure was conducted, the most notable observation is that the SR-30 got increasingly louder as the RPM was increased. Furthermore, the increased speed of the engine was visible in the behaviour of the flame in the combustor, which became increasingly stretched as the RPM increased.

2.5 Experimental Data

Figure 2.1

This graph shows the relationship between the RPM of the SR-30 and its Isentropic Efficiency

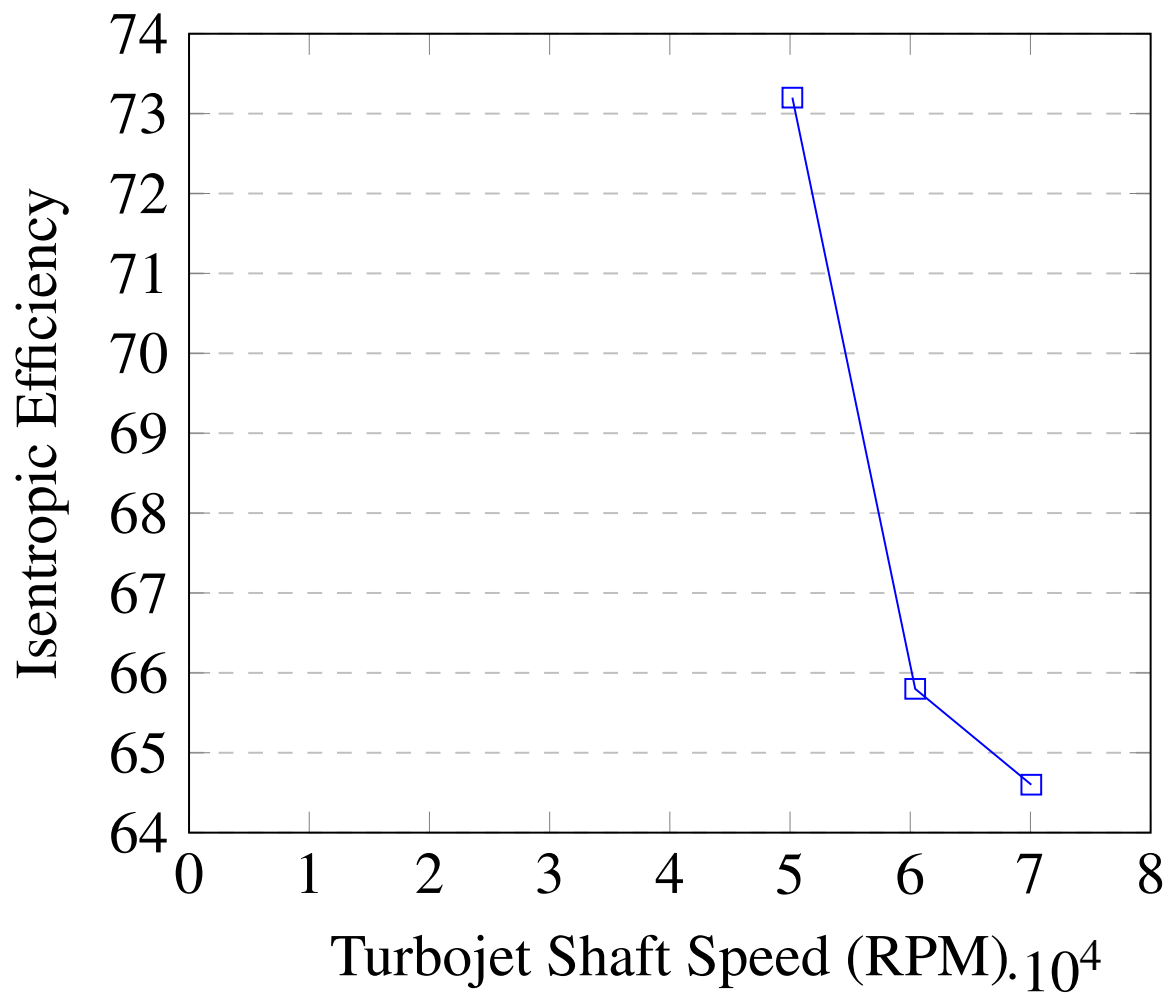


Figure 2.2

This graph shows the relationship between the Pressure Ratio of the SR-30 and it's Isentropic Efficiency

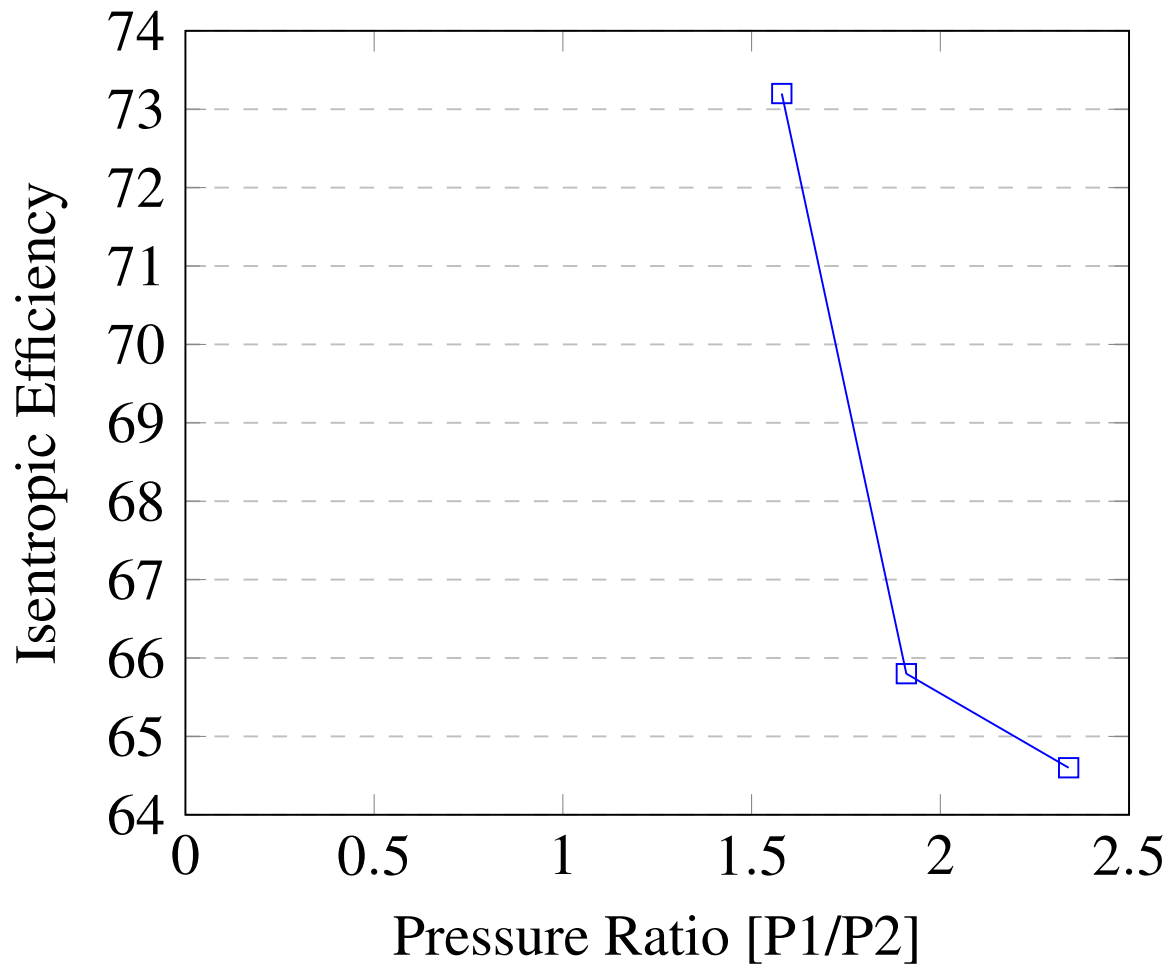


Figure 2.3

This graph shows the relationship between the entropy drop in the compressor and the exit temperature of the compressor.

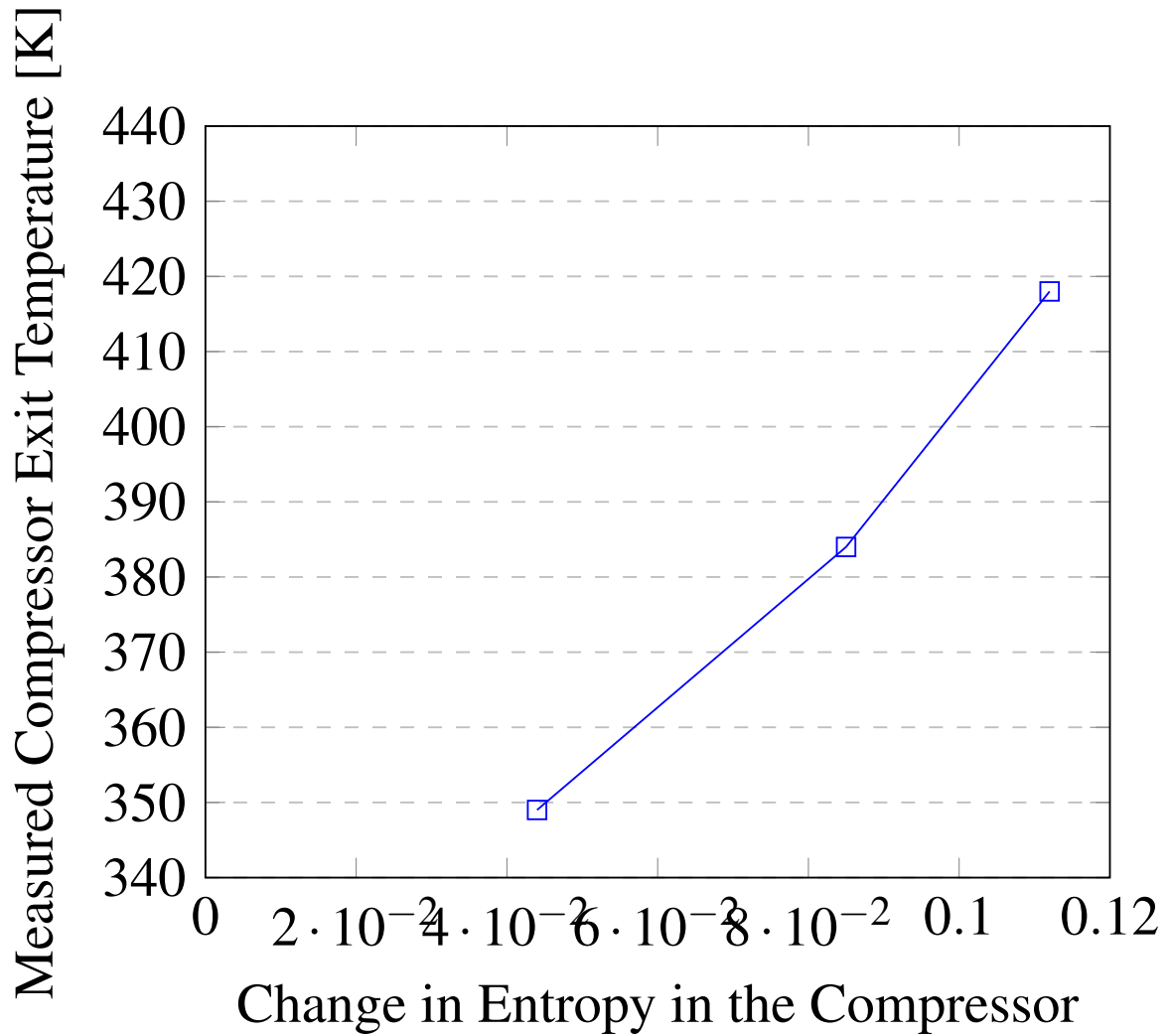


Figure 2.4

This graph shows the relationship between the RPM of the SR-30 and it's Brayton Cycle Efficiency

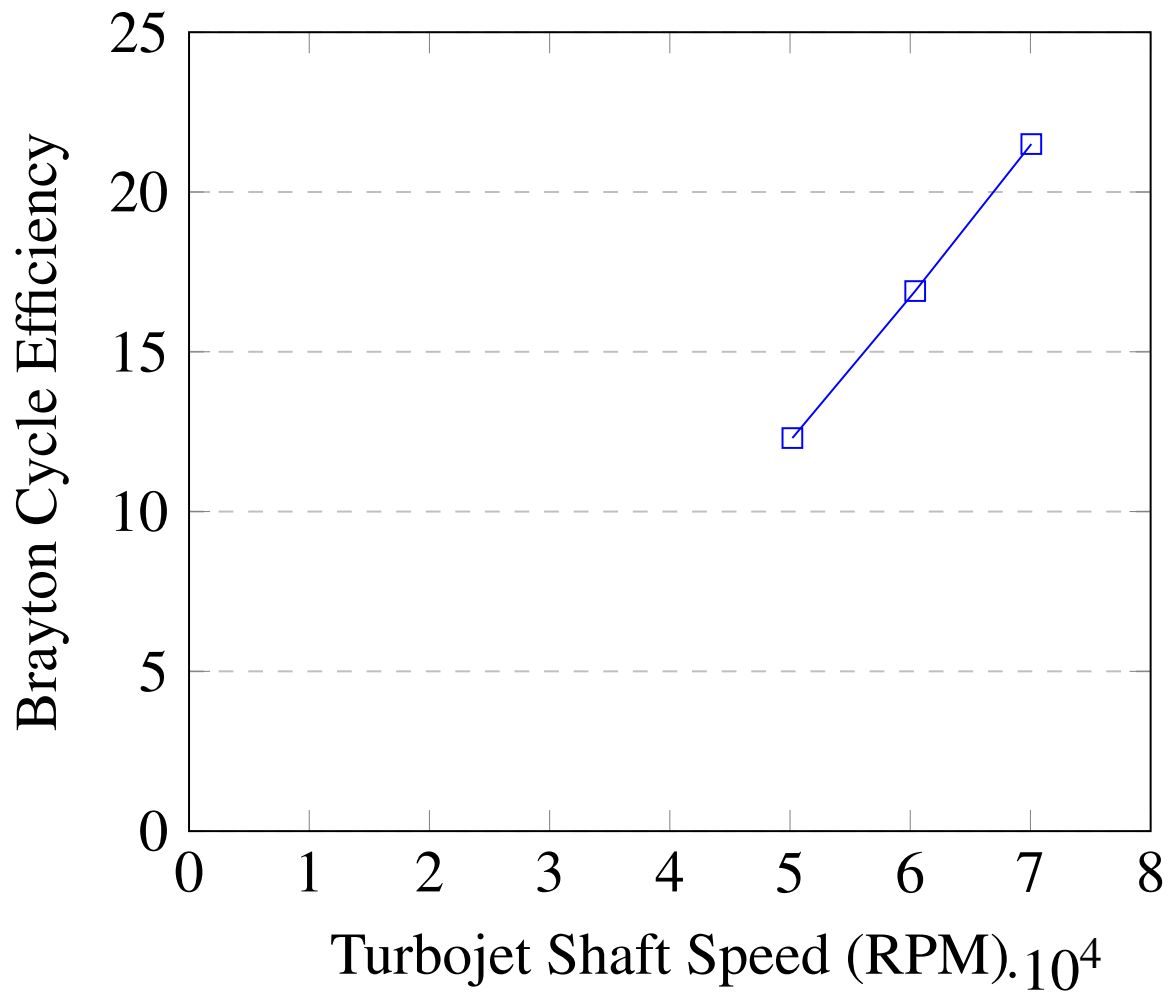


Figure 2.5

This graph shows the relationship between the RPM of the SR-30 and it's Measured Thrust

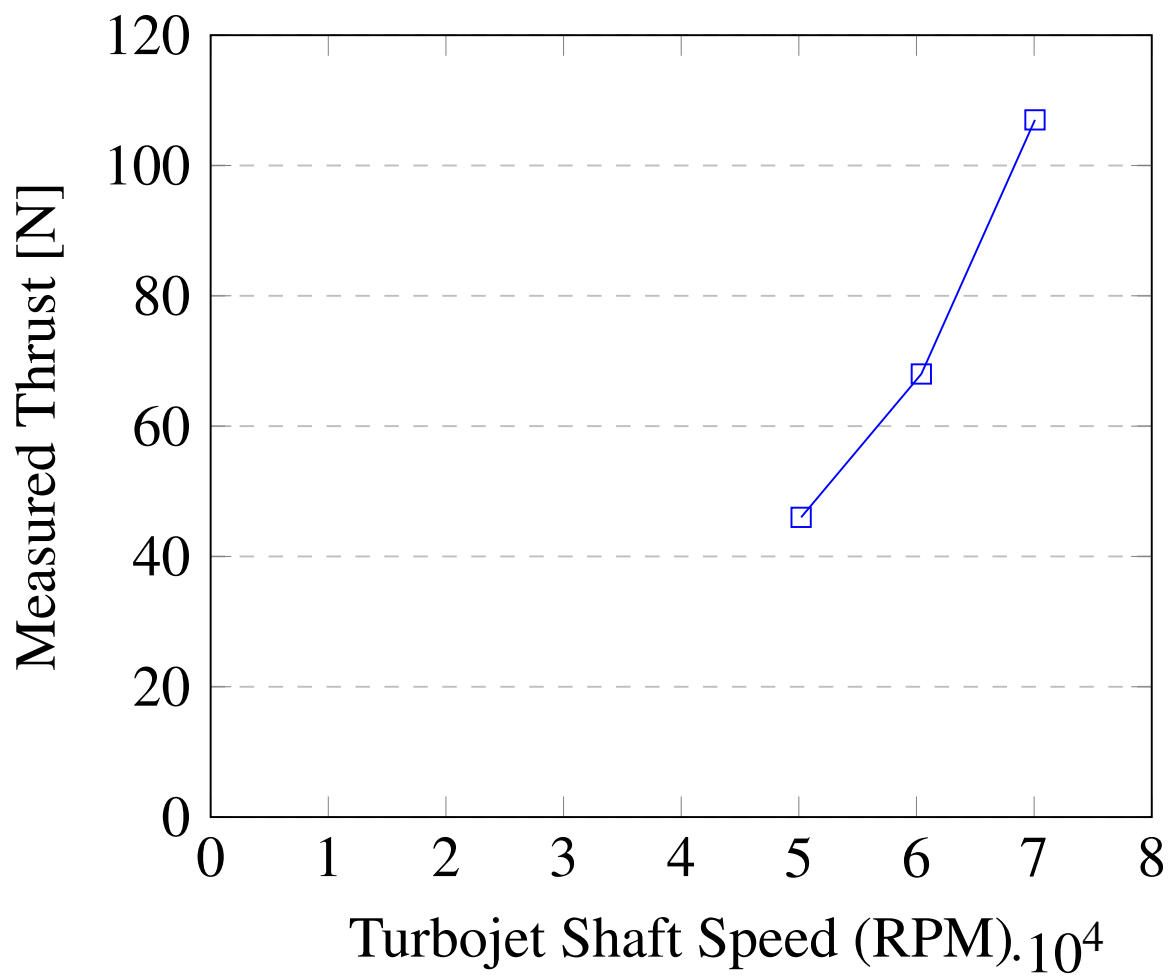


Figure 2.6

This graph shows the relationship between the RPM of the SR-30 and it's TSFC

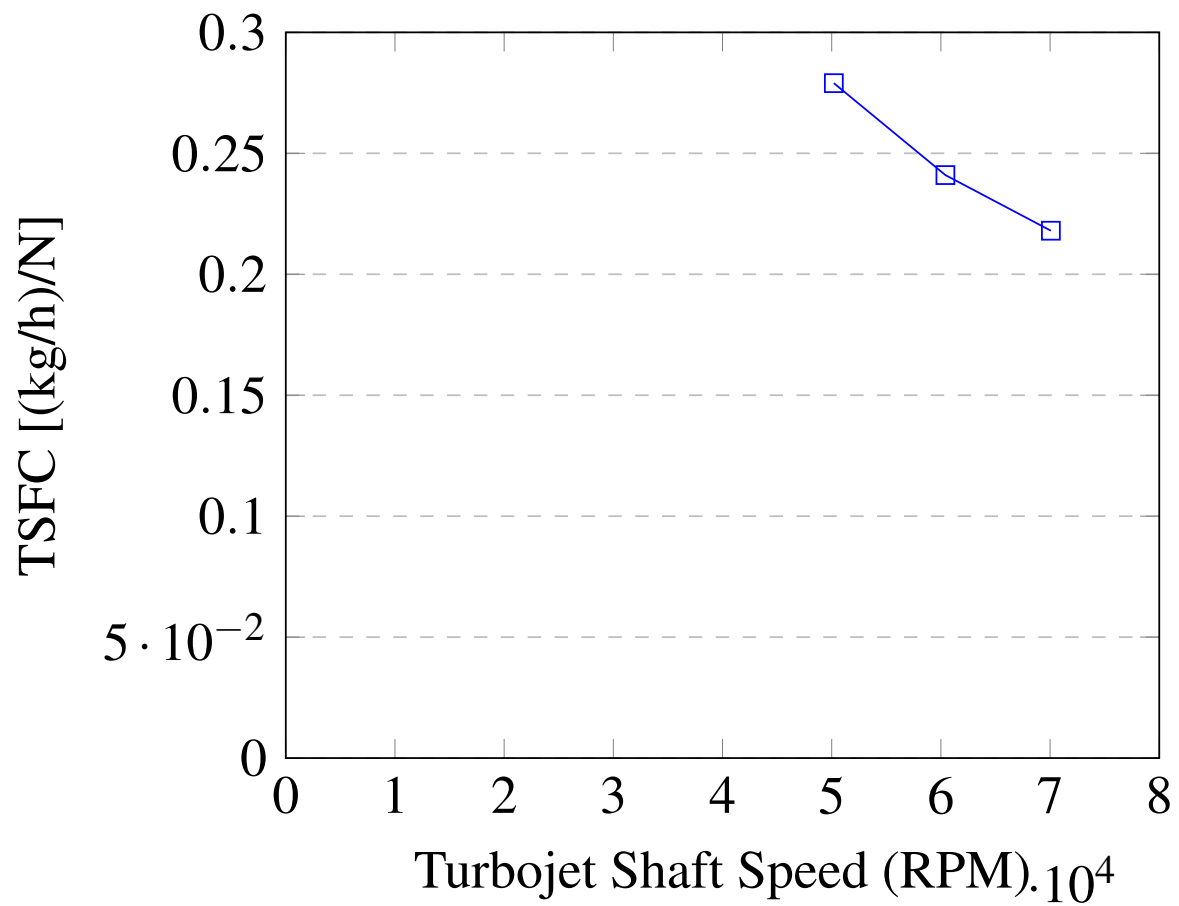


Figure 2.7

This graph shows the relationship between the RPM of the SR-30 and it's Nozzel Exit Mach Number.

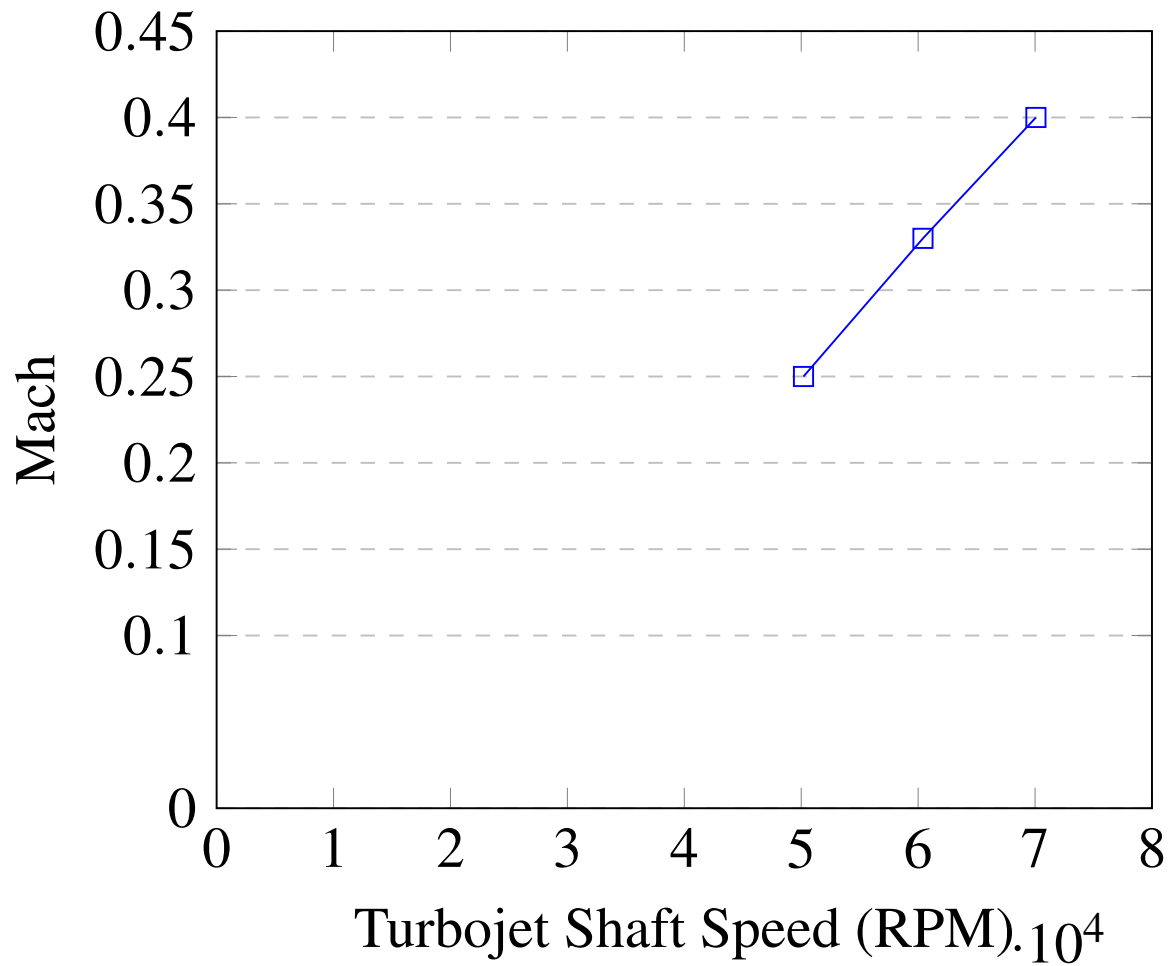
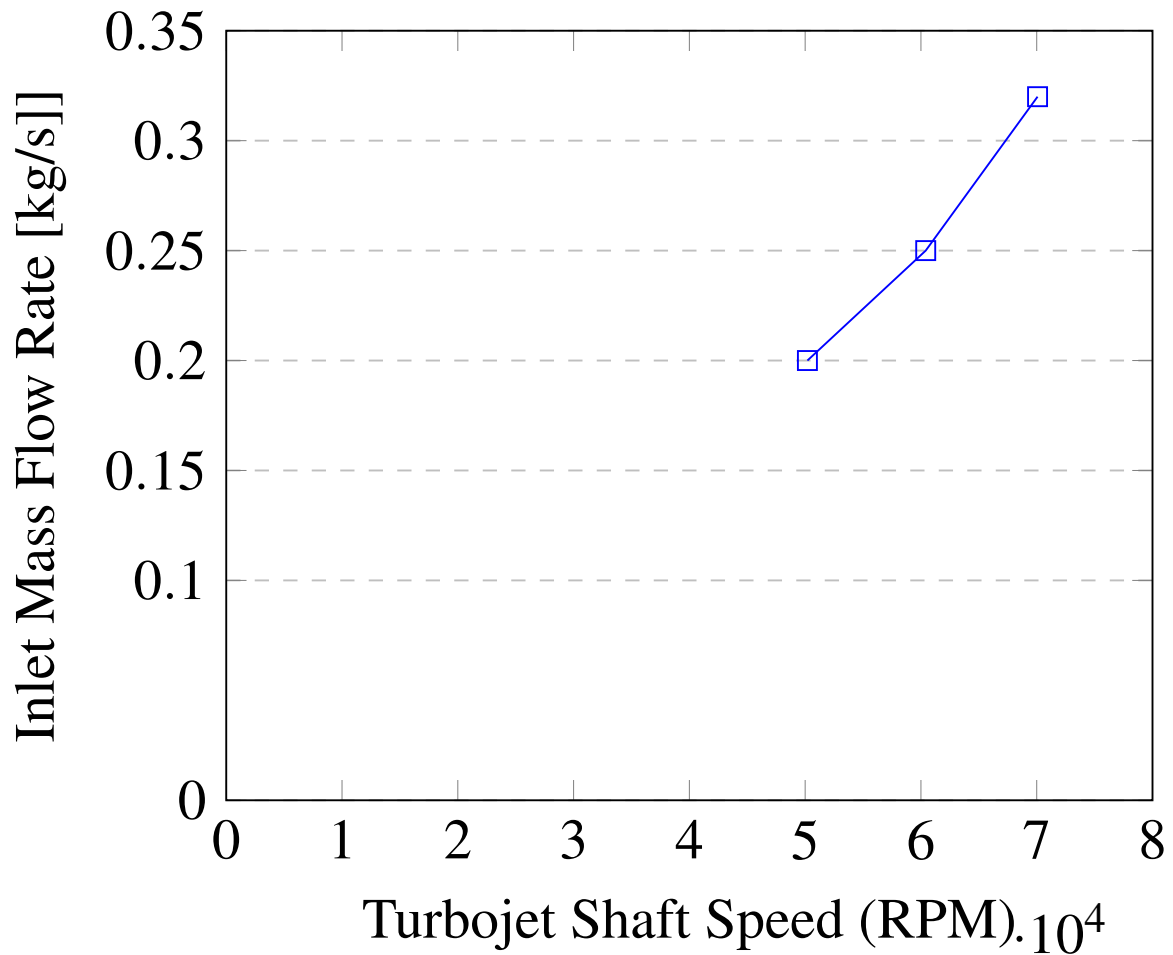


Figure 2.8

This graph shows the relationship between the RPM of the SR-30 and it's Inlet Mass Flow Rate

**Table 2.1**

This table shows the values of thrust for the SR-30, both measured and calculated with increasing RPM.

RPM	Calculated Thrust at Exit	Measured Thrust
	(N)	(N)
50195	23	46
60413	42	68
70073	63	107

2.6 Post-Processing Methodology

When calculating parameters based on the measured results obtained, we assume that the process is completely isentropic. Therefore, all calculations will be completely ideal values for each parameter. The isentropic efficiency however can be obtained for this engine, at various different engine speeds, as seen in Figure 2.1. This equation is obtained by:

$$\eta = \frac{T_{2s} - T_1}{T_2 - T_1}, \quad (2.1)$$

Where T_{2s} is the Isentropic Temperature at the compressor exit and T_1 and T_2 are the temperatures at the compressor inlet and exit respectively. Ultimately, the value of Thrust can be calculated by knowing the mass flow rate (\dot{m}) at the nozzle outlet and the airspeed at the nozzle outlet (v). This is assuming a stationary engine, which the SR-30 was and the nozzle area is 0.0025m.

$$T = \dot{m} \times v, \quad (2.2)$$

$$\dot{m} = \rho \times A \times v, \quad (2.3)$$

$$v = \sqrt{\frac{2(P_0 - P_{static})}{\rho}} \quad (2.4)$$

2.7 Discussion

Figure 2.6 shows the relationship between RPM and TSFC. From this graph, it can be seen that an inverse exponential relationship exists between the two parameters. This means that the TSFC decreases at a non-constant rate as RPM increases, which means that the SR-30 overall performs more efficiently at higher RPMs. Furthermore, an exponential relationship also exists between RPM and measured Thrust (as seen in Figure 2.5), as RPM increases

Thrust also increases at a non-constant rate. This means that not only is the engine more efficient at higher RPMs, it also produces more thrust. This suggests that aircraft that use this engine would be more performant at higher flight speeds. Figure 2.4 shows that the relationship between RPM and Brayton cycle efficiency is linear, as the RPM increases, the Brayton cycle for the SR-30 becomes more efficient. In fact, from an RPM of 50000 to 70000, the efficiency increases from 12.3% to 21.5%. Figure 2.7 also shows a linear relationship for the Mach number at the exit from the nozzle and RPM, this makes logical sense, as the engine speed increases, the airflow speed also increases. The Mach number raises from 0.25 at 50000 RPM to 0.4 at 70000 RPM. Again, the relationship is the same for the Inlet Mass flow rate and RPM. The mass flow rate increases by 0.12Kg/s as the RPM of the SR-30 increases, which again makes logical sense. As the SR-30 burns more fuel due to higher RPM, the airspeed inside the engine increases. This means that the increased fuel and higher speed both contribute to an increased mass flow rate through the compressor inlet of the engine.

The values of the calculated thrust are much higher than the thrust measured by the TTL Mini-Lab. This does not make logical sense, as we know that calculations assume 100% isentropic conditions and from Figure 2.1 a significant drop in isentropic efficiency is observed as the SR-30's RPM is increased. Therefore, we would expect the values of Thrust to be significantly lower than those found by calculating in Table 2.1. There are many potential reasons for this error ,including:

- The TTL Mini-Lab's thrust gauge is not properly calibrated.
- Vibrations from running the engine will artificially raise the thrust experienced by the thrust gauge.
- Human error in gathering the data from the computer system.
- Each of these factors could explain why the measured values of thrust are significantly higher than would be expected. However, it is likely a combination of all these factors, and others, that have led to the errors encountered in this procedure.

2.8 Conclusions

To conclude, the procedure was successfully conducted to analyse the SR-30 turbojet engine located in the laboratory, values of Thrust for different RPMs were both measured and calculated. Data produced by this procedure also shows that the engine performs more efficiently at higher values of RPMs. Finally, the data was analysed as the discrepancies between measured and calculated values were discussed and explained as limits of the procedure. Overall, the procedure's aims and objectives, to analyse the performance of the SR-30 and understand the Brayton Cycle, were successfully achieved.

3 Appendix

Equation 1.1 is used to calculate the shock angles as discussed in the main body of this report and is recalled here:

$$\tan(\theta) = 2\cot(\beta) \frac{M^2 \sin^2(\beta) - 1}{M^2(\gamma + \cos(2\beta) + 2)} \quad (3.1)$$

Since the equation must be solved for β an iterative process was used to find values. Microsoft Excel was chosen for this task due to its ease of use. For each value of flow angle θ , a value for its tangent was found and then the right hand side was computed for various values of β until a matching value to 4 decimal places was found.

References

British Standards Institution. (2020). Hearing protectors – general requirements – earplugs.

<https://knowledge.bsigroup.com/products/hearing-protectors-general-requirements-earplugs>

Clancy, L. J. (1986). *Aerodynamics*. Pitman Publishing.

<https://archive.org/details/aerodynamics0000clan>